# Self-propelled supramolecular nanomotors with temperature-responsive speed regulation

# Self-propelled Supramolecular Nanomotors with Temperature-Responsive Speed Regulation

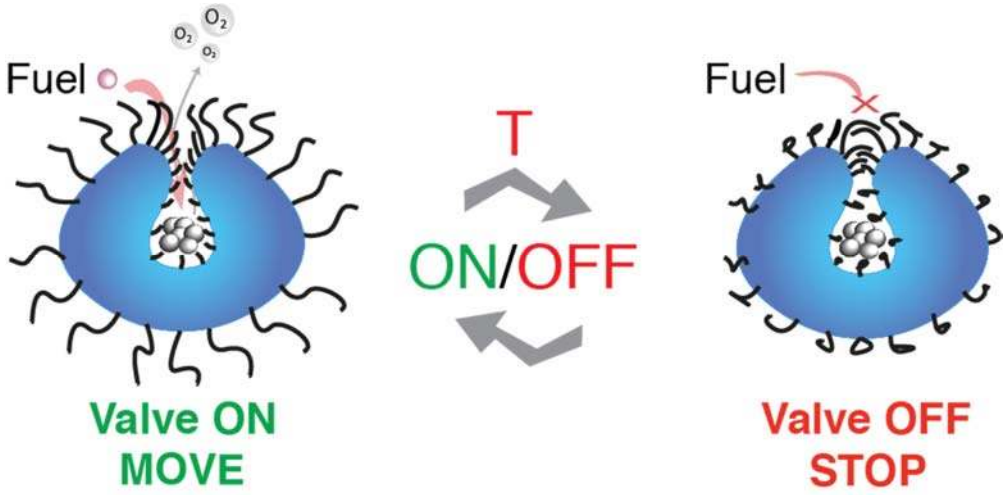


This work has been published in:

Tu, Y.; Peng, F.; Sui, X.; Men, Y.; White, P. B.; van Hest, J. C. M.; Wilson, D. A. Self-propelled supramolecular nanomotors with temperature-responsive speed regulation. Nat. Chem. 2016, doi:10.1038/nchem.2674

**Abstract**

Self-propelled catalytic micro- and nanomotors have been the subject of intense study over the past few years, but it remains a continuing challenge to build in an effective speed-regulation mechanism. Movement of these motors is generally fully dependent on the concentration of accessible fuel, with propulsive movement only ceasing when the fuel consumption is complete. In this chapter we report a demonstration of control over the movement of self-assembled stomatocyte nanomotors via a molecularly built, stimulus-responsive regulatory mechanism. A temperature-sensitive polymer brush is chemically grown onto the nanomotor, whereby the opening of the stomatocytes is enlarged or narrowed on temperature change, which thus controls the access of hydrogen peroxide fuel and, in turn, regulates movement. To the best of our knowledge, this represents the first nanosized chemically driven motor for which motion can be reversibly controlled by a thermally responsive valve/brake. We envision that such artificial responsive nanosystems could have potential applications in controllable cargo transportation.

## 1 Introduction

Recent advances in artificial micro- and nanomotors[1-3] have brought their potential applications in the biomedical sciences closer[4-9]. Starting from the first centimeter-scale motors[10], micro- and nano-tubular engines[11-14], wires[15,16], helices[17,18], rods[19-21], Janus motors[22-24] and self-assembled polymeric motors[8,25-27] scientists used both top-down or bottom-up approaches to design motors with high speeds and improved efficiency. These classes of motors can convert chemical fuel (such as hydrogen peroxide[21,28-30], hydrazine[31], acid[32,33], water[34], glucose[27,35] and urea[24]) or external energy such as magnetic fields[17,36,37], ultrasound[19,38], electricity[39,40], light[41-43] or even organisms[44] into mechanical motion[45]. Recently, new avenues to control the directionality of the nanomotors by mimicking taxis behavior inspired by nature were shown. These types of systems are however still based on external factors for the directional control of motion such as the presence of a gradient[8]. One of the limitations of current micro- and nanomotor systems is therefore still the limited control over their speed[46-49]. Some level of manipulation of the movement of micron-sized motors was previously achieved either by disassembling the whole micromotor under a thermal stimulus[47] or by chemically inhibiting the catalytic enzymatic system[49]. The latter required sequential steps of inhibition and reactivation via addition of chemicals followed by multiple washings, which is not very practical for biomedical applications. Motor systems would be more versatile if equipped with a molecularly built stimuli-responsive valve or brake[50], thus controlling and regulating the motion under the stimuli without changing the shape or assembly of the motor itself or by affecting its catalytic activity. Such property is particularly desirable for applications in the biomedical field and nanorobotics.

In our previous work, we demonstrated the formation of self-assembled nanomotors, based on bowl-shaped polymer vesicles, known as stomatocytes, in which catalytic platinum nanoparticles were entrapped[25]. The narrow opening of the bowl shape structures serves as an outlet for the oxygen generated during the catalytic decomposition of the hydrogen peroxide fuel. Hydrogen peroxide is found naturally in the human body, especially in diseased areas such as tumor tissue and sites of inflammation. According to the literature[51], human tumor cell lines can produce hydrogen peroxide at rates of up to 0.5 nmol/$10^4$ cells/h which is significant when related to the size of the tumor. Therefore nanomotor systems running on low concentrations of hydrogen peroxide with further ability to sense changes in the environment and regulate their speed and behavior via a stimuli-responsive valve or brake would be very attractive for biomedical

applications.

In this chapter we demonstrate the first nanomotor system with complete control over its speed by chemically attaching a stimulus-responsive valve system (polymer brush) to our engine that allows control of the motion of the nanovesicles without changing the catalyst activity or shape of the motor (Fig. 1). This doesn't require the addition of chemicals into the system but instead the nanomotor is able to probe the environment and change its behavior by sensing the change in the outside temperature. Stimulus-responsive polymer brushes[52] made of surface-tethered macromolecules are commonly known and have been widely applied in many areas, including the biomedical field[53-55]. Changes in the external environment (e.g., temperature, pH, light or redox states) can generally trigger a sharp and large response in the structure and properties of these grafted polymer layers[56]. Various polymer brushes have been synthesized via the SI-ATRP approach on different substrates using surface-attached initiators[57], which allows accurate control of the structure and properties of the polymer brushes.

By functionalizing the surface of the stomatocytes with a poly(*N*-isopropyl acrylamide) (PNIPAM) polymer brush via SI-ATRP a temperature-responsive polymer layer is introduced. Due to PNIPAM's well-known LCST behavior[58], increasing the temperature above its transition temperature leads to the collapse of the brushes, producing a hydrophobic layer on top of the small opening of the stomatocytes (less than 5 nm); this closes the aperture and prevents easy access of the fuel (hydrogen peroxide) inside the nanomotor (Fig. 1c, d). Due to the lack of fuel, the propelling movement of the motor will cease. The long molecularly built brushes function as a reversible brake system onto the nanomotors by controlling and regulating the access of the fuel inside the catalytic bowl shape structures with temperature. As the LCST behavior is reversible, by adjusting the temperature, the collapse of the PNIPAM brushes can be switched on and off, functioning thus as a regulatory mechanism to control the speed of the nanomotor (Fig. 1). This is in our view an elegant example of a brake system that doesn't affect the catalytic activity or the shape of the motor but only its motion. It is also the closest mimic of a brake as found in automated cars from the macroscopic world.

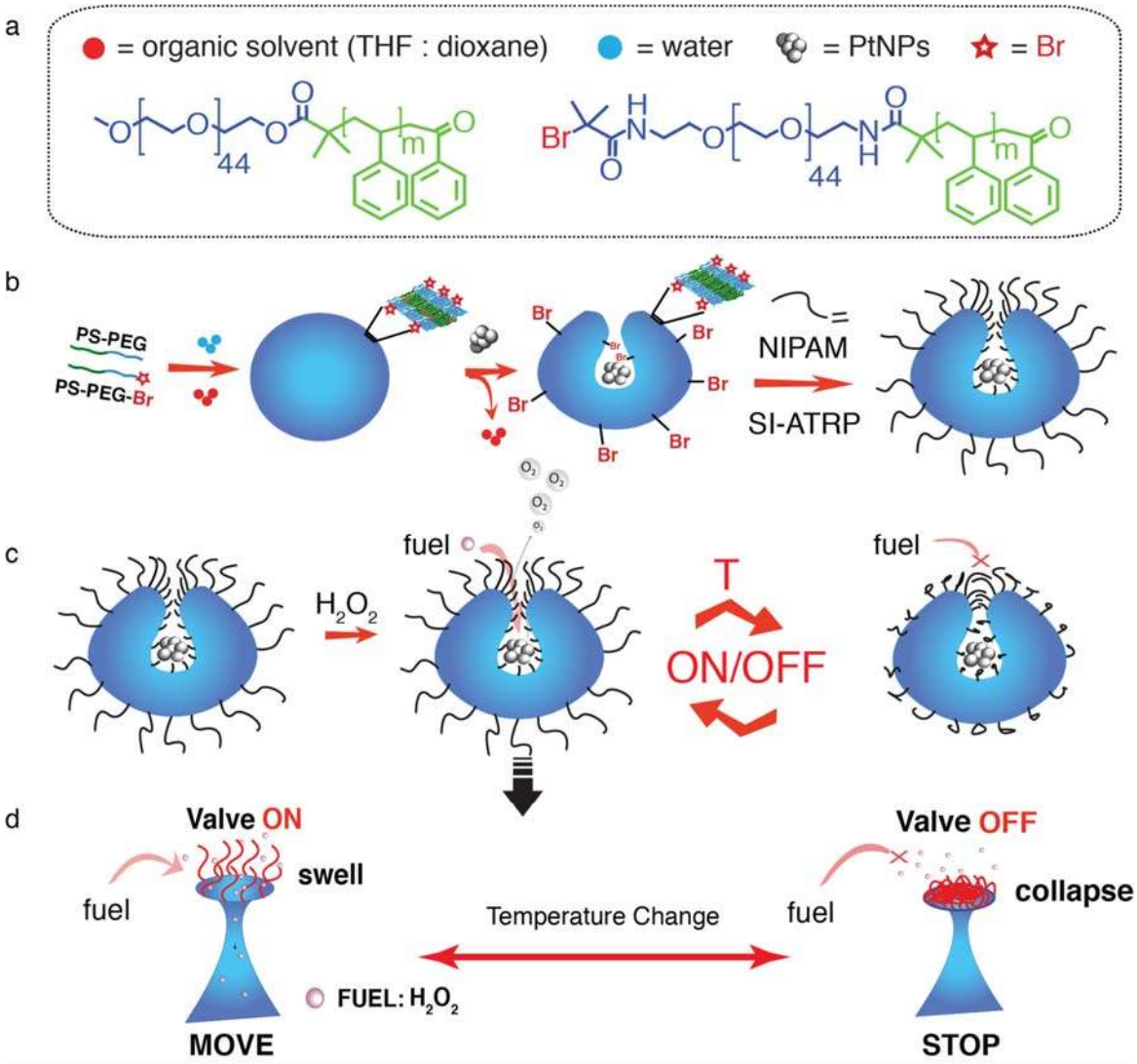


**Figure 1 | Fabrication of polymeric stomatocyte nanomotors with thermo-sensitive brakes.** **a,** Chemical structure of block copolymer PEG-*b*-PS and functionalized polymer Br-PEG-*b*-PS used for stomatocyte assembly. The polymers were synthesized via ATRP of styrene starting from a PEG macroinitiator. **b,** Schematic representation of the formation of PtNPs-loaded stomatocytes with ATRP initiator (PtNPs-Stoma-Br) and the subsequent growth of PNIPAM brushes by SI-ATRP on the surface of the stomatocytes. Polymersomes are formed by the self-assembly of PEG-*b*-PS and Br-PEG-*b*-PS in organic solvent. PtNPs were added subsequently and then entrapped during the shape transformation to form PtNPs-Stoma-Br. PtNPs-Stoma-Brush were obtained after polymerization of PNIPAM brush in 10% methanol for 30 min. **c** and **d,** Schematic representation of reversible control over the speed of PNIPAM modified stomatocyte motors by changing the temperature. Collapse of PNIPAM brushes takes place resulting in the covering of the opening of stomatocytes when the temperature is increased above the LCST of PNIPAM.

## 2 Results and discussion

**Assembly of the Motor and Chemical Attachment of the Valve.** Polymeric stomatocytes with ATRP initiator moieties on the surface, were prepared by mixing poly(ethylene glycol)-*b*-polystyrene ($PEG_{44}$-*b*-$PS_{212}$, PDI=1.07), prepared via standard ATRP procedures, with α-bromo ester functional-poly(ethylene glycol)-*b*-polystyrene (Br-$PEG_{44}$-*b*-$PS_{238}$, PDI=1.20). After confirming successful attachment of the ATRP initiator onto the polymer by 2D Nuclear Magnetic Resonance Spectroscopy (2D-NMR, Heteronuclear Multiple Bond Correlation, Fig. 2), the block copolymers were dissolved in an organic solvent mixture (THF: dioxane = 4: 1, V/V). MilliQ water was subsequently slowly added into the solution resulting in the self-assembly into flexible polymersomes. PtNPs were then entrapped during the shape transformation upon dialysis from thermodynamically stable spherical morphologies to the kinetically bowl-shaped stomatocytes. After vigorous dialysis for at least 48 hours to remove the organic solvent and vitrify the membrane, PtNPs-loaded stomatocytes (PtNPs-Stoma) and PtNPs-loaded stomatocytes with ATRP initiators (PtNPs-Stoma-Br) on the surface were obtained. From dynamic light scattering (DLS), no significant difference in the size of the structures was observed after introducing the ATRP initiator. (See Table 1)

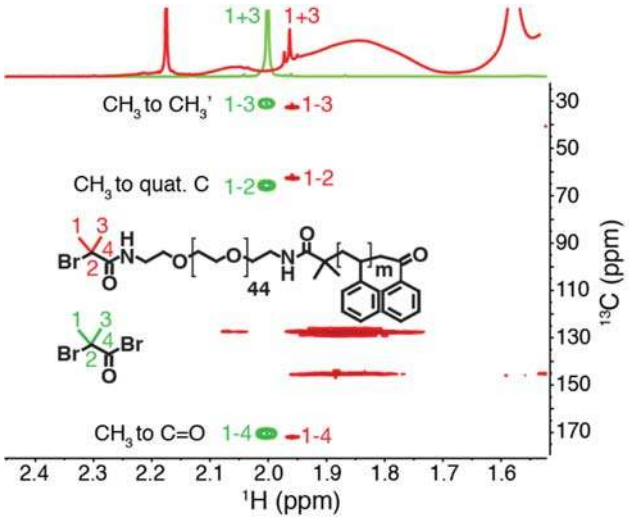


**Figure 2 | Characterization of functional polymer Br-PEG-*b*-PS.** Comparison of Heteronuclear Multiple Bond Correlation (HMBC) signal of Br-PEG-*b*-PS (red) with that of α-bromoisobutyryl bromide (green). As shown in Figure 2, the HMBC signal of the methyl group (1) from Br-PEG-*b*-PS (red) correlated with the other methyl group (3, $\delta_{13C}$=32.50 ppm), the quaternary carbon (2, $\delta_{13C}$=62.90 ppm) and the neighboring carbonyl group (4, $\delta_{13C}$=172.27 ppm). The significant shift of the signals compared to that of non-conjugated α-bromoisobutyryl bromide (green, $\delta_{13C}$=30.95 ppm, 65.99 ppm and 170.64 ppm respectively), confirmed the successful attachment of the ATRP initiator onto the polymer.

**Table 1. Size of Stomatocytes and Stomatocytes after growing brush**

| | Before growing brush/nm | After growing brush/nm |
|---|---|---|
| 0% PtNPs-Stoma-Br | 337 (PDI=0.150) | 434 (PDI=0.062) |
| 10% PtNPs-Stoma-Br | 341 (PDI=0.177) | 689 (PDI=0.060) |

Cryo-Transmission Electron Microscopy (Cryo-TEM) measurements at different angles (Fig. 3a) showed that PtNPs were indeed encapsulated in the cavity of the stomatocyte. Transmission electron microscopy (TEM) analysis confirmed the formation of stomatocytes with similar small openings for both stomatocytes (Fig. 3b) and also the encapsulation of PtNPs (Fig. 3c).

In order to switch the motors on and off in a controllable fashion, thermo-sensitive PNIPAM brushes were grown onto the surface of PtNPs-Stoma-Br by SI-ATRP, using 10 mol% of initiator functional PEG-*b*-PS (PEG-*b*-PS: Br-PEG-*b*-PS=9:1). The polymerization of the PNIPAM brushes took place in 10% methanol solution (v/v) with CuBr/PMDETA as catalyst/ligand under argon pressure for 30 min. After dialysis for 2 days, PtNPs-loaded stomatocytes with PNIPAM brushes (PtNPs-Stoma-Brush) were obtained. To confirm the successful growth of the polymer brushes, the structures were characterized by using several imaging techniques. Transmission electron microscopy images showed the presence of stomatocyte motors with rough surfaces, most probably due the growth of the PNIPAM brushes. (Fig. 3d) The size of the stomatocyte nanomotors, measured by DLS at room temperature (Table 1), also increased accordingly after SI-ATRP from 341 nm to 689 nm, indicating again the presence of PNIPAM brushes. The average length of the PNIPAM brushes was furthermore calculated using $^{1}$H-NMR spectroscopy. Stomatocytes with PNIPAM brushes (Stoma-Brush) were freeze-dried after dialysis and the resulting stomatocyte powder was dissolved and measured by $^{1}$H-NMR. After SI-ATRP for 30 min, the degree of polymerization of PNIPAM brushes was determined to be 769, while the molecular weight was approximately 85kDa (Molecular weight of PNIPAM was calculated according to the ratio between PS and PNIPAM).

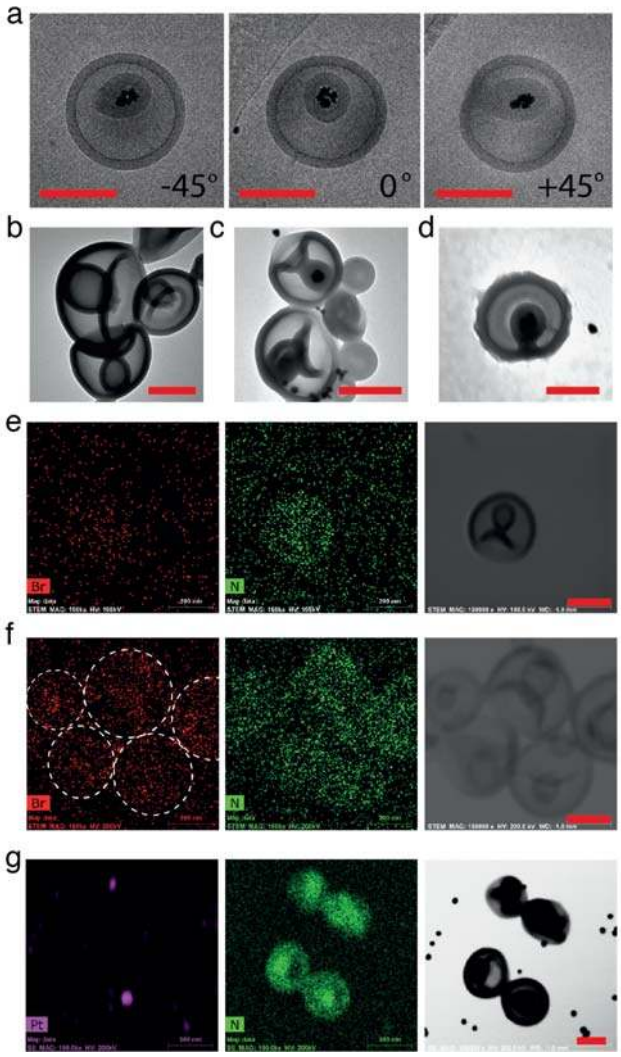


**Figure 3 | Characterization of Stoma, Stoma-Br, PtNPs-Stoma and PtNPs-Stoma-Brush. a,** Cryo-TEM measurements of PtNPs-Stoma (same vesicle) at different angles, namely -45°, 0° and 45°, which demonstrated that PtNPs were indeed loaded in the cavity of stomatocyte; **b,** TEM measurements of Stoma-Br; **c,** TEM image of PtNPs-Stoma-Br; **d,** TEM image of PtNPs-Stoma-Brush; **e,** EDX signals of Stoma with element of Br (red) and N (green); **f,** EDX signals of Stoma-Br with element of Br (red) and N (green); **g,** EDX signals of PtNPs-Stoma-Brush with element of Pt (purple) and N (green). Scale Bar: 200 nm.

In order to obtain further confirmation of the presence of the PNIPAM brushes, Energy-dispersive X-ray spectroscopy (EDX) was used to map the presence of certain elements on the stomatocytes. Significant Br enrichment was found for the mixed stomatocytes (Stoma-Br) (Fig. 3f) compared to normal stomatocytes without ATRP initiator present (Stoma) (Fig. 3e). After the growth of PNIPAM brushes on the stomatocytes, N enrichment was also observed due to the amide moieties in the NIPAM monomers (Fig. 3g).

To fully confirm the covalent attachment of the PNIPAM to the stomatocytes we used diffusion NMR to measure the diffusion coefficients of PNIPAM on the self-assembled Stoma-Brush compared to free PNIPAM. Due to the high viscosity of deuterium oxide ($D_2O$), Methanol-D4 (MeOD) was used for diffusion measurements, in which the stomatocytes also proved to be stable. From Fig. 4, resonances specific to PNIPAM in the sample of Stoma-Brush at around 1.20 ppm and 4.00 ppm were observed. The PEG-*b*-PS block copolymers were not visible due to their self-assembled state and the coverage with PNIPAM. After fitting the decay curve of the NMR intensity, the diffusion coefficient of the PNIPAM brushes on the stomatocytes was determined to be $6.09*10^{-8}$ $cm^2/s$ (Fig. 4d). The diffusion coefficient of free PNIPAM (molecular weight: 23k Da) obtained in MeOD was $9.93*10^{-7}$ $cm^2/s$ (Fig. 4b).

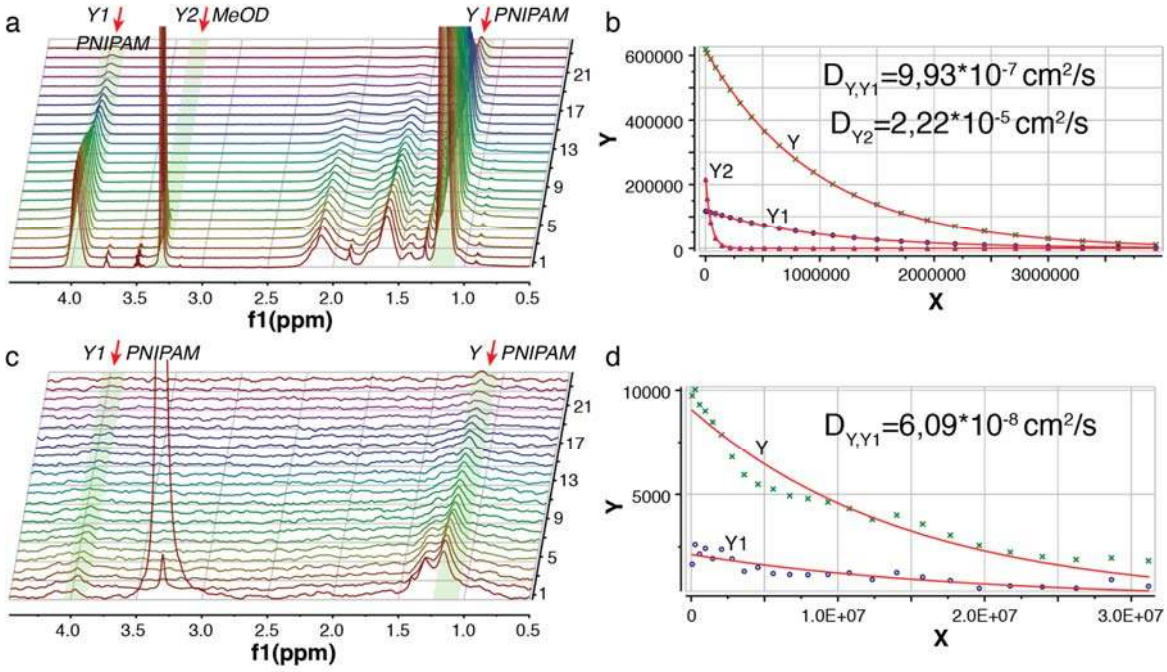


**Figure 4 | Diffusion NMR measurements of free PNIPAM and Stoma-Brush in MeOD. a,** Diffusion NMR spectrum of free PNIPAM (23k Da) in MeOD; **b,** Fitting curve of the diffusion coefficient of free PNIPAM (23k Da); **c,** Diffusion NMR spectrum of Stoma-Brush in MeOD; **d,** Fitting curve of the diffusion coefficient of Stoma-Brush. PNIPAM peaks at around 1.2 ppm and 4.0 ppm were observed from the NMR spectrum. After fitting with the equation (Mono-exponential Fit, B+exp(-x*F)), $D_Y$ (diffusion coefficient from PNIPAM at 1.2 ppm) and $D_{Y1}$ (diffusion coefficient from PNIPAM at 4.0 ppm) were obtained. $D_{Y,Y1}$ was the average of $D_Y$ and $D_{Y1}$. $D_{Y2}$ was the diffusion coefficient from MeOD at 3.3 ppm. The diffusion coefficient of free PNIPAM with 23k Da was 16 times higher than that of grown PNIPAM brushes, showing the covalent linkage of PNIPAM layer on the surface of stomatocytes.

When a higher molecular weight of free PNIPAM (100k Da) was used, the diffusion coefficient of PNIPAM was lowered slightly, as expected, to $6.48*10^{-7}$ $cm^2/s$ (See Fig. 5a,b). As the diffusion coefficient of PNIPAM brushes attached to the stomatocyte is more than one order of magnitude smaller compared to free PNIPAM, this is a clear indication that the PNIPAM brushes are indeed chemically linked to the stomatocyte. To make sure this observation is not caused by physical interaction of the brushes with the surface of the self-assembled structures, we also performed diffusion NMR on a physical mixture of Stoma and free PNIPAM (23k). The diffusion coefficient obtained was around $7.77*10^{-7}$ $cm^2/s$ (See Fig. 5c,d), which was similar to free PNIPAM, confirming that free PNIPAM does not significantly interact with the surface of stomatocytes.

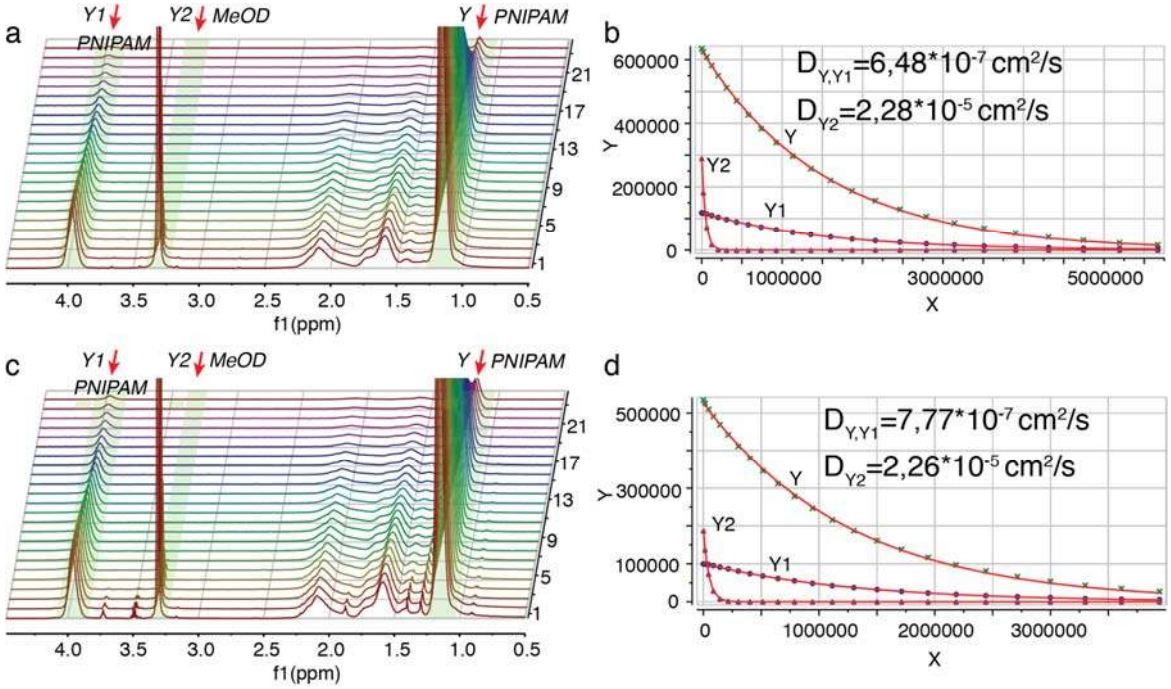


**Figure 5 | Diffusion NMR measurements**. **a,** Diffusion NMR of free PNIPAM (100k) in MeOD; **b,** Fitting curve of diffusion coefficient of free PNIPAM (100k); **c,** Diffusion NMR of mixture of Stoma and free PNIPAM (23k) in MeOD; **d,** Fitting curve of diffusion coefficient of mixture of Stoma and free PNIPAM (23k). PNIPAM peaks at around 1.2 ppm and 4.0 ppm were observed from the NMR spectrum. After fitting with the equation (Mono-exponential Fit, B+exp(-x*F)), $D_Y$ (diffusion coefficient from PNIPAM at 1.2 ppm) and $D_{Y1}$ (diffusion coefficient from PNIPAM at 4.0 ppm) were obtained. $D_{Y,Y1}$ was the average of $D_Y$ and $D_{Y1}$(4.0 ppm). $D_{Y2}$ was the diffusion coefficient from MeOD at 3.3 ppm. The diffusion coefficient of MeOD was much lower than that of PNIPAM as expected. The diffusion coefficients of MeOD obtained from different measurements were almost the same, which indicated nice repeatability of diffusion NMR.

The formation of PNIPAM brushes was further confirmed by Fourier Transform infrared spectroscopy (FT-IR); specific peaks of PNIPAM around 3650-3120 $cm^{-1}$ ($OH_{str}$, $NH_{str}$) and

1700-1400 $cm^{-1}$ ($C=O_{str}$, amide) appeared in the IR spectrum after SI-ATRP and were comparable with the literature[59]. After establishing the chemical structure of the PtNPs-Stoma-Brush, the particles were heated above the LCST of PNIPAM to experience a collapse of the polymer brushes. Using DLS measurements, as expected the size of the stomatocytes decorated with PNIPAM brushes decreased sharply from 689 nm to 453 nm after heating (from 25 ºC to 40 ºC, especially around 35 ºC, the LCST of PNIPAM) (Fig. 6a)

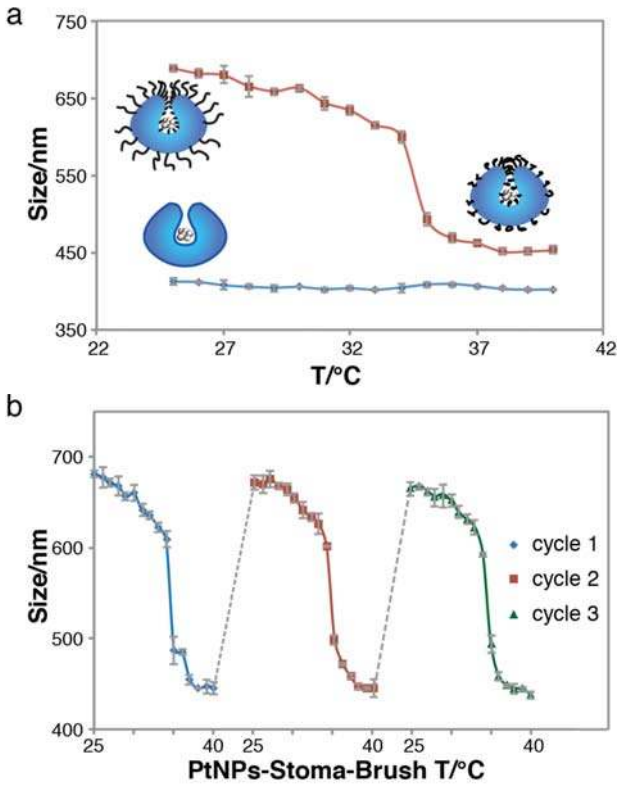


**Figure 6 | Characterization of PNIPAM brushes on stomatocytes. a,** Temperature effect on the sizes of PtNPs-Stoma and PtNPs-Stoma-Brush. The difference in sizes between PtNPs-Stoma and PtNPs-Stoma-Brush were compared during heating from 25 ºC to 40 ºC. Error bars indicate the standard deviation of three replicating measurements; **b,** Three heating cycles of PtNPs-Stoma-Brush from 25 ºC to 40 ºC. Size of PtNPs-Stoma-Brush was measured during the heating cycle by DLS. Another heating cycle was operated after cooling to room temperature of the same sample. Error bars indicate the standard deviation of three replicating measurements.

No obvious size change was observed for normal stomatocytes, the size only slightly decreased from 412 nm to 403 nm during the temperature increase. The reversible temperature-responsive behavior of the PNIPAM brushes was also confirmed by DLS measurements, showing three identical heating and cooling cycles (from 25 ºC to 40 ºC) for the PtNPs-Stoma-Brush. (Fig. 6b)

The PtNPs-Stoma-Brush proved to be colloidally stable as long as they were kept at a temperature below the LCST of PNIPAM. Strong aggregation and irreversible behavior was observed only when the samples were kept above the LCST of PNIPAM for several days. This is most probably due to interaction between the hydrophobic PNIPAM brushes.

To demonstrate the formation of a hydrophobic layer around the stomatocyte when the particles were heated above the LCST of PNIPAM and the ability to regulate the access of the fuel, the hydrophobic Nile red was used as model dye. Nile red is almost non-fluorescent in water but undergoes fluorescence enhancement and large absorption and emission blue shifts in hydrophobic environments. Small amounts of Nile red in DMF were mixed with Stoma-Brush ($3.8 \times 10^{11}$ particles/mL, measured by Nanosight) and also with normal Stoma ($3.9 \times 10^{11}$ particles/mL, measured by Nanosight, similar concentration as for Stoma-Brush), and the fluorescence intensities of both samples were measured at different temperatures. We expected that the hydrophobic Nile Red would enter into hydrophobic layer formed by the PNIPAM brush on the surface of the stomatocytes at higher temperatures (above LCST). At 40 ºC, the fluorescence intensity of Stoma-Brush (mixing with Nile red) increased almost 70% because of the presence of the hydrophobic PNIPAM, while the intensity of normal Stoma (with Nile red ) showed only 36% enhancement due to the increased solubility of Nile red at higher temperature. (Fig. 7) When the system was cooled back to 30 ºC, the intensity of the Stoma-Brush decreased by 30% compared to that of normal Stoma (due to the release of Nile red from the PNIPAM layer). Compared to the intensity at 30 ºC in the beginning, both samples had higher fluorescence intensity most probably because the extra amount of Nile red dissolved in the solution at 40 ºC did not seed out when the temperature went back to 30 ºC. Reversiblity in hydrophilic-hydrophobic properties of PNIPAM brushes was thus confirmed during the Nile red experiment.

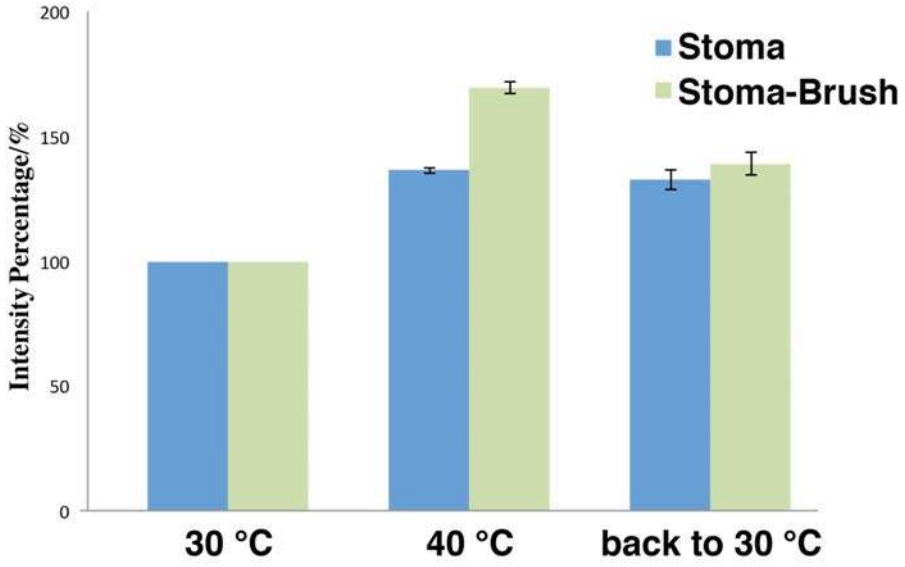


**Figure 7 | Mixing Stoma and Stoma-Brush with hydrophobic Nile red at different temperatures.**

**Testing the functioning of the Valve/Brake on the nanomotor.** After confirming the temperature responsiveness of the PNIPAM brushes on the stomatocyte nanomotors, we next set out to investigate whether this behavior could be used to introduce a temperature-sensitive regulatory mechanism for the movement of the nanomotors. Nanoparticle-tracking analysis was used to record in real-time the movement of stomatocyte motors in hydrogen peroxide solution by video recording the movement of the nanomotors for 90 seconds, each second containing 30 frames. Furthermore, the NTA technique allows for the simultaneous recording of the x,y coordinates of multiple particles which were further used in plotting the average mean square displacement curves of 20 particles. A 4.98 mM hydrogen peroxide solution was used, in which PtNPs-Stoma (non-functionalized) were dispersed, and the resulting solution was measured at 30ºC. Fitting of the mean-square displacements (MSD) curves allows for calculation of the average speed of the nanomotors by using the self-diffusiophoretic model proposed by Golestanian and coworkers[60]. The MSD (Fig. 8c) and speed (Fig.10a) of the nanomotors in the presence of hydrogen peroxide fuel showed directional autonomous movement as was demonstrated in our previous studies.[25] When the temperature was increased to 40ºC, the velocity and MSDs increased due to higher catalytic efficiency of PtNPs towards hydrogen peroxide (See Fig. 10a and Fig. 8c). In addition, no visible bubbles were observed during the measurement under these conditions. When the same experiment was repeated with PtNPs-Stoma-Brush,

slightly lower speeds (Fig. 10a and Fig. 9) were observed at 30 ºC when compared to the non-functionalized nanomotors. We think this is due to the lower access and penetration of hydrogen peroxide through the PNIPAM brushes. However, when PtNPs-Stoma-Brush was investigated at 40 ºC a complete hindrance of the autonomous movement of the nanomotors was observed. The MSD curve showed a typical shape and size for Brownian motion, which was similar to the behavior of non-functionalized nanomotors at 40 ºC in the absence of fuel (Fig. 8b).

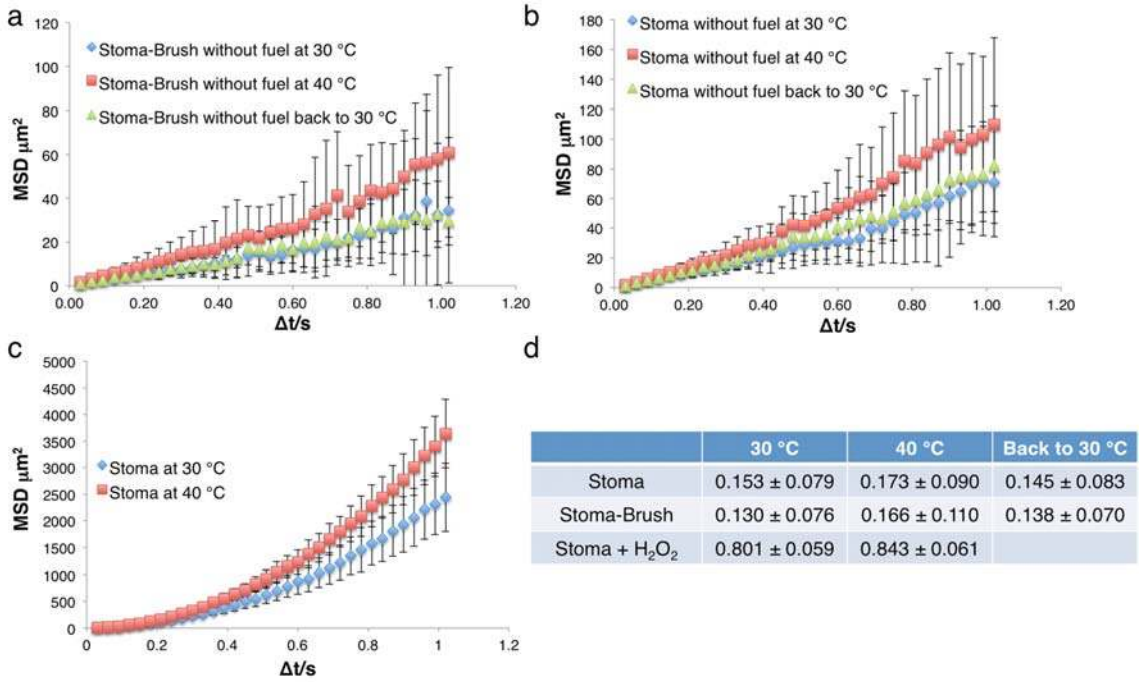


| | 30 °C | 40 °C | Back to 30 °C |
|---|---|---|---|
| Stoma | 0.153 ± 0.079 | 0.173 ± 0.090 | 0.145 ± 0.083 |
| Stoma-Brush | 0.130 ± 0.076 | 0.166 ± 0.110 | 0.138 ± 0.070 |
| Stoma + $H_2O_2$ | 0.801 ± 0.059 | 0.843 ± 0.061 | |

**Figure 8 | MSD and directionality of stomatocyte nanomotors. a,** MSD of PtNPs-Stoma-Brush without $H_2O_2$; **b,** MSD of PtNPs-Stoma without $H_2O_2$; **c,** MSD of PtNPs-Stoma with $H_2O_2$; **d,** directionality of PtNPs-Stoma-Brush without $H_2O_2$, PtNPs-Stoma with $H_2O_2$ and PtNPs-Stoma without $H_2O_2$. The directionality was calculated by comparing the Euclidian distance to the accumulated distance, which represents a measurement of the directionality of trajectories. Software Chemotaxis and Migration Tool 2.0 from Ibidi Company was used for directionality calculation.

We think this is because the collapsed PNIPAM brushes on the surface of the nanomotors hinder diffusion of hydrogen peroxide into the cavity. When the temperature was lowered to 30 ºC (below the LCST), PNIPAM brushes re-swelled to be water soluble, and hydrogen peroxide fuel could reenter into the cavity of stomatocytes motors. PtNPs started to decompose the hydrogen peroxide again to propel the structures.

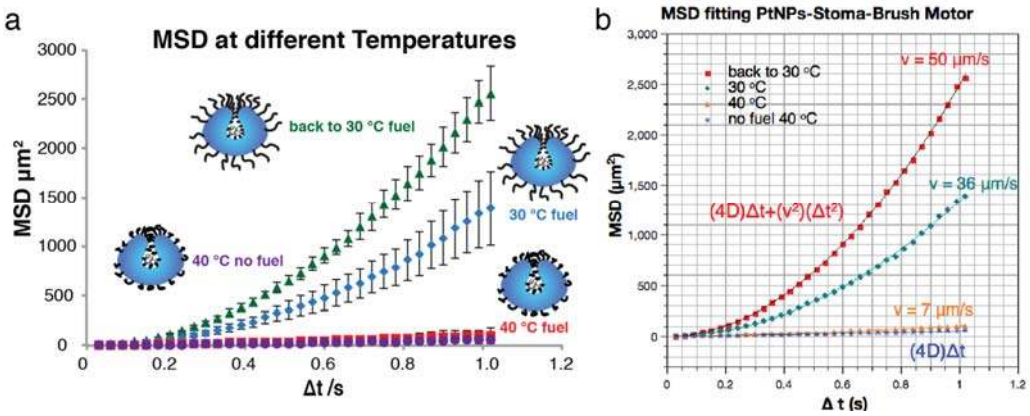


**Figure 9 | Average MSD and MSD fitting of PtNPs-Stoma-Brush in the presence of Hydrogen peroxide fuel.** "Δt" is not the total time of the video recording and particle monitoring but instead the time difference used for measuring the deviation over time between the position of the particle and the reference position, which is typically plotted in a MSD graph. The velocity of a directed motion was extracted from the fitting of the MSD curve by using the equation $(4D)\Delta t+(v^2)(\Delta t^2)$ while for a Brownian motion , the MSD show only a linear fitting according to the equation $(4D)\Delta t$.

Interestingly, after one cycle of closing the valve, and returning to 30 ºC, the motors moved at larger speeds compared to the starting point (Fig.10a). Possible reasons for this behavior might be that during the first cycle a cleaning of the catalyst occurred and consequently the efficiency of the PtNPs was improved, which was further confirmed by determination of the catalytic efficiency of PtNPs (Fig. 11).

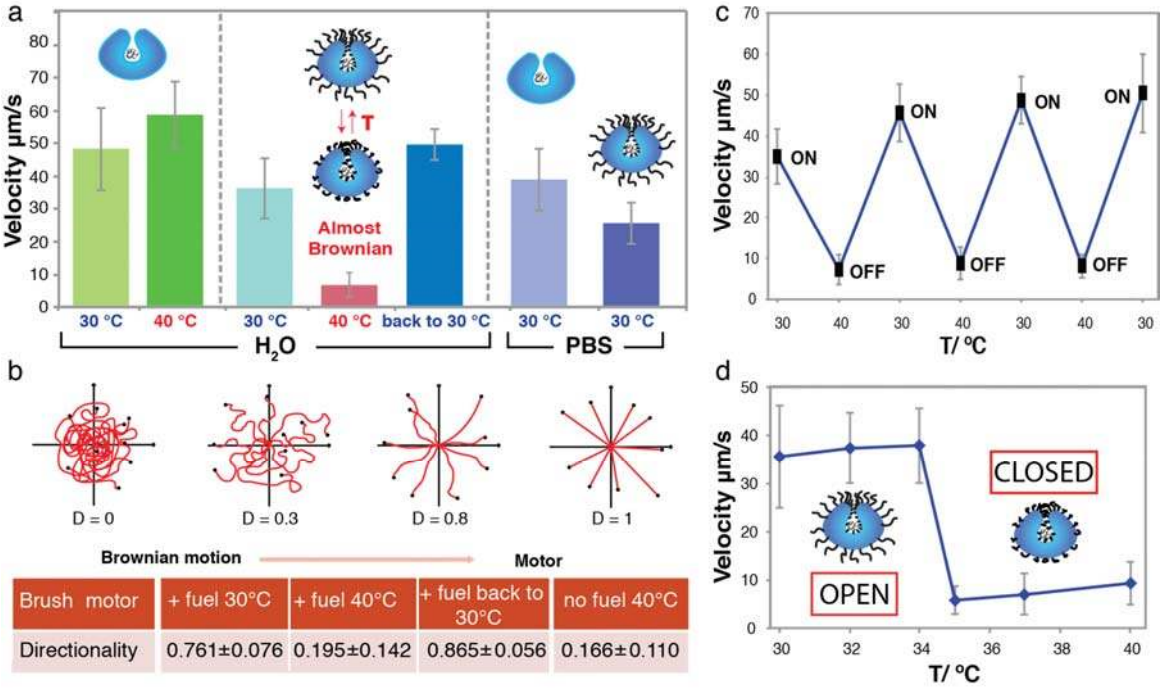


| Brush motor | + fuel 30°C | + fuel 40°C | + fuel back to 30°C | no fuel 40°C |
|---|---|---|---|---|
| Directionality | 0.761±0.076 | 0.195±0.142 | 0.865±0.056 | 0.166±0.110 |

**Figure 10 | Motion evaluation of PtNPs-Stoma-Brush and PtNPs-Stoma. a,** Velocity of PtNPs-Stoma-Brush/ PtNPs-Stoma in presence of $H_2O_2$ at different temperatures and also in different media. 30 μL hydrogen peroxide (final concentration was 4.98 mM) was added into 1 mL motor solution, and the motion of the nanomotors was measured at different temperatures and in different media by Nanosight NS 500. Velocities were calculated respectively. Directional motion was fitted using the equation $(4D)\Delta t + (v^2)(\Delta t^2)$, and Brownian motion was fitted using equation $(4D)\Delta t$. Error bars indicate the standard deviation of the velocity of 20 motors; **b,** Directionality of PtNPs-Stoma-Brush at different temperatures. The directionality was calculated by comparing the Euclidian distance to the accumulated distance, which represented a measurement of the directionality of trajectories. Software Chemotaxis and Migration Tool 2.0 from Ibidi Company was used for directionality calculation; **c,** three ON-OFF cycles of PtNPs-Stoma-Brush. Error bars indicate the standard deviation of the velocity of 20 motors; **d,** the motion of PtNPs-Stoma-Brush in presence of $H_2O_2$ at different temperatures. Error bars indicate the standard deviation of the velocity of 20 motors.

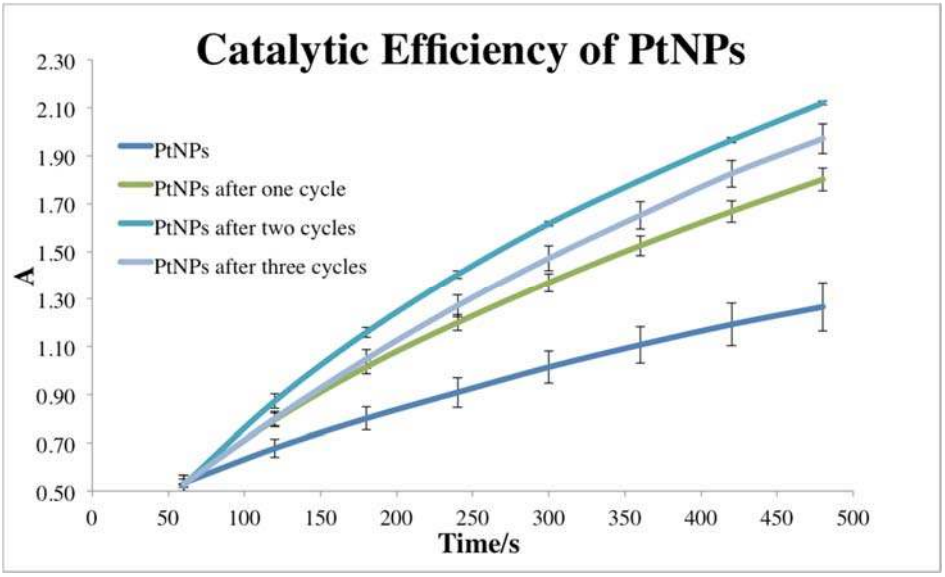


**Figure 11 | Catalytic efficiency of PtNPs solution after cycles.** The catalytic efficiency of PtNPs increased after cycles.

According to the mechanism of motion studied, we think there are two different possible mechanisms in our system, namely self-diffusiophoresis and bubble propulsion. In our previous study[8,25,27,61], we have found that the motion is largely affected by the concentration of the fuel and also depends on the type of the catalyst incorporated inside of the stomatocyte structures. In addition, a recent study showed that both high catalytic activity and the rough surface of platinum particles/film are necessary to change the propulsion mode from self-diffusiophoresis to bubble propulsion[62]. In our case, the PtNPs are branched structures and have rough surfaces, which also

indicate the preference for the bubble propulsion mechanism at higher fuel concentrations. Extra experiments were performed to investigate the mechanism of motion for our nanomotor before and after attaching the valve system. It is well known that electrolyte diffusiophoresis based on ionic gradients generated by hydrogen peroxide decomposition can be suppressed in a highly concentrated electrolyte solution.[7] Therefore the movement of stomatocyte nanomotors with a valve in PBS was measured and MSD was also calculated afterwards. After MSD fitting, the speed in the presence of $H_2O_2$ of the stomatocyte nanomotors with a valve in PBS was lower than that of the motor in MilliQ water (Fig.10a). However, it was still higher than the speed of the motors without $H_2O_2$, which also indicated the higher probability for the bubble propulsion mechanism, since visible bubbles were seen at higher concentration of $H_2O_2$. Based on the previous evidence and the latest studies we expect our system would form bubbles, however they should be nanobubbles. Furthermore, the pinning and growth of the bubbles should start from the catalyst surface, which in our case is hidden inside of the nanocavity of the stomatocyte. In addition it could be that the slowing down effect observed in buffer is also due to the change in the conformation of the brushes resulting from the interaction of the salts with the brush valve. This could result in a partial closing of the valve system, which diminishes the transfer of the fuel through the opening. We tested this by measuring the size of the valve motor in water and PBS with DLS. Only a small difference of around 2 nm in size was observed suggesting a minimal change in the availability of fuel (Table 2).

**Table 2. Size of PtNPs-Stoma-Brush in PBS and water**

| | PBS/nm | Water/nm |
|---|---|---|
| PtNPs-Stoma-Brush | 678.7 (PDI=0.074) | 680.1 (PDI=0.107) |

The directionality was also calculated to give more information about the motion of our nanomotor system by comparing Euclidean and accumulated distances[28]. A directionality of D=1 indicates a straight-line migration from start to endpoint (Fig. 10b). The directionality of the PtNPs-Stoma-Brush at 40 ºC in presence of $H_2O_2$ was 0.195 (final concentration was 4.98 mM, 20 particles tracking), which was much lower than that of PtNPs-Stoma-Brush at 30 ºC. Such small values indicate the occurrence of a Brownian motion, which was also confirmed by the

shape of the trajectories of the nanomotors. Due to reversible LCST behavior of PNIPAM brush, the "ON−OFF" motion control cycle is repeatable and reproducible, as demonstrated in Fig.10c. In order to figure out whether we can partially block the access of $H_2O_2$ fuel to slow down the motion without completely stopping the motion with the temperature, the motion of PtNPs-Stoma-Brush at 30, 32, 34, 35, 37 and 40 ºC respectively was measured. Below the LCST of PNIPAM brush (LCST of PNIPAM was between 34-35 ºC), the velocity and MSDs of motors at 34 ºC increased because of the elevated efficiency of the encapsulated catalyst compared to that at 30 ºC. However, PtNPs-Stoma-Brush stopped completely when the system was heated up to 35 ºC. In our case, the polymer brush was synthesized via surface-initiated ATRP, which led to dense and high molecular weight PNIPAM. In addition, PNIPAM brushes responded very fast to temperature changes, which also led to the inability to partially slow down the speed of motors. To gain more insight into the movement mechanism we also plotted the speed of PtNPs-Stoma-Brush vs time (Fig. 12). The velocity of the motor remained similar at the beginning due to high enough surrounding $H_2O_2$ fuel, while the speed started to drastically decrease after 16 min. The shape of the speed/time curve also indicates the presence of two possible mechanisms of motion, bubble propulsion at high $H_2O_2$ fuel concentration and self-diffusiophoresis at low $H_2O_2$ concentration.

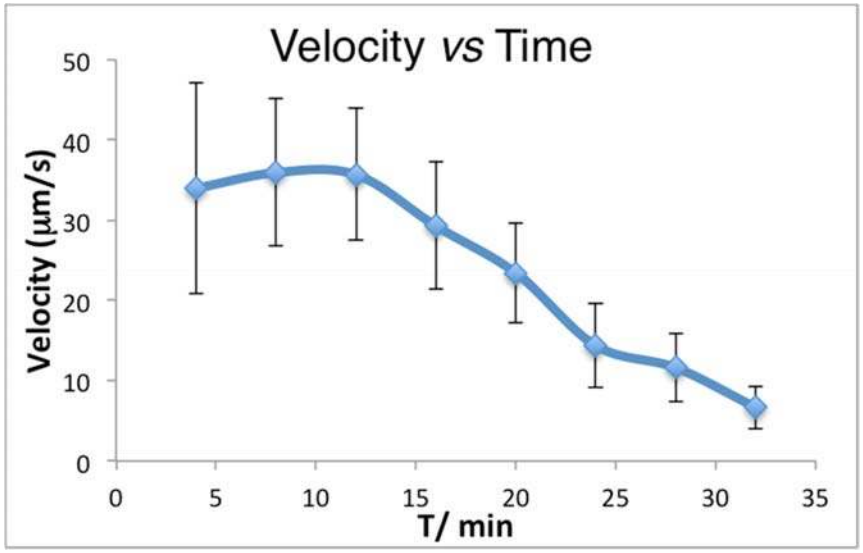


**Figure 12 | The velocity of PtNPs-Stoma-Brush in time.** The velocity of motors was calculated according to MSDs fitting by the equation $(4D)\Delta t+(v^2)(\Delta t^2)$.

## 3 Conclusions

In summary, PtNPs-loaded supramolecular stomatocyte nanomotors with thermo-sensitive valves based on PNIPAM brushes were prepared. DLS, IR, EDX, TEM and diffusion NMR results confirmed that PNIPAM brushes were on the surface of the stomatocytes and that they could reversibly respond to changes in temperature. Furthermore, the autonomous movement of our PtNPs-Stoma-Brush system could reversibly be switched on and off by crossing the LCST of PNIPAM in the presence of the hydrogen peroxide fuel. Our nanomotor system is molecularly built and this is as far as we know the first example of a nanomotor with a molecular valve that can control its speed. The system is in effect able to locally sense the environment (in this case temperature) and regulate the accessibility of the fuel and accordingly adjust its speed and behavior. Our system has wide implications not only from a fundamental point of view, which is control of movement at the nanoscale but also from the perspective of applications, for instance as potential locomotive drug carriers where size and control of movement are two important aspects of a controllable cargo transportation. In addition, we believe that this type of brake system can be applied not only to motion regulation but also to controlled release of drugs from the cavity of stomatocytes. We envision that such artificial responsive nano-systems could have potential applications in delivery applications.

## 4 Acknowledgements

This work was supported by the European Research Council under the European Union's Seventh Framework Programme (FP7/2007-20012)/ERC-StG 307679 "StomaMotors". We acknowledge support from the Ministry of Education, Culture and Science (Gravitation program 024.001.035). F. Peng acknowledges funding from the China scholarship council. Geert-Jan Janssen and the General Instruments department are acknowledged for providing support for the Cyro-TEM and EDX measurements.

## 5 Supplementary Information

### 5.1 Materials

Unless stated otherwise, all reagents and chemicals were used without further purification. Styrene (Sigma-Aldrich) was distilled before polymerization to remove the inhibitor. *N*-isopropyl acrylamide from Sigma-Aldrich was purified by repeated recrystallization in a mixture of toluene/hexane (50:50, v/v). CuBr (Sigma-Aldrich) for ATRP was washed with acetic acid and followed by methanol (MeOH) for three times and stored under Ar. Tetrahydrofuran (THF) for reaction was distilled under Argon from sodium/benzophenone. Ultra pure MilliQ water obtained from a MilliQ QPOD purification system (18.2 MΩ) was used for self-assembly and dialysis of polymersomes/stomatocytes. Spectra/Por® Dialysis Membrane MWCO: 12-14,000 g/mol was used for dialysis of polymersomes/stomatocytes. Polyvinyl pyrrolidone (PVP, Mn 10 kg/mol), poly(ethylene glycol) methyl ether (Mn 2 kg/mol), α-ω-amino-poly(ethylene glycol) (Mn 2 kg/mol), L (+) ascorbic acid, magnesium sulfate, sodium bicarbonate, potassium tetrachloroplatinate (II), sodium chloride, ethylenediaminetetraacetic acid (EDTA), 1-phenyl-1-trimethylsiloxyethene, α-bromoisobutyryl bromide, (Benzotriazol-1-yloxy)tripyrrolidinophosphonium hexafluorophosphate (PyBOP), chloroform-d ($CDCl_3$), methanol-d4 (MeOD), *tert*-butyl α-bromoisobutyrate, N,N,N',N'',N''-pentamethyldiethylenetriamine (PMDETA), dimethylformamide (DMF) and 3,3',5,5'-tetramethylbenzidine (TMB) were purchased from Sigma-Aldrich. THF, anisole and N,N-diisopropylethylamine (DIPEA) were obtained from Acros. MeOH, hydrochloric acid (37%), triethylamine and hydrogen peroxide were purchased from J.T. Baker. Diethyl ether (Carlo Erba Reagents), 1,4-dioxane (Biosolve BV), dichloromethane ($CH_2Cl_2$, Fisher Chemical) and Nile red (Chem Impex) were also used.

### 5.2 Instruments

Routine NMR spectra were recorded on a Varian Inova 400 spectrometer with $CDCl_3$ as a solvent. Diffusion measurements were performed at 298 K on a Bruker Avance III 500 MHz spectrometer equipped with a BBFO probe. The maximum z-gradient for the probe is 53.5 G/cm. Diffusion measurements were calibrated to pure methanol and ethylene glycol. The pulse sequence incorporated delays for eddy currents to dissipate and bipolar gradients for encoding and

decoding diffusion information. Malvern Zetasizer Nano S was used for dynamic light scattering (DLS) analysis with the following settings: temperature 25 °C, He-Ne laser wavelength 633 nm and detector angle 173°. For transmission electron microscopy, a JEOL 1010 Transmission Electron Microscope with MegaView Soft Imaging camera at an acceleration voltage of 60 kV was used. Cryogenic transmission microscopy was performed on a JEOL TEM 2100 with high-quality Gatan 895 ultrascan 4000 bottom mount camera (4080x4080 pixels). Energy-dispersive X-ray element mapping was done on a Bruker Quantax EDS system with an STEM detector incorporated. Nanoparticle tracking analysis (NTA) of stomatocyte nanomotors was performed on a NanoSight NS500.

### 5.3 Synthetic procedures, self-assembly and characterizations

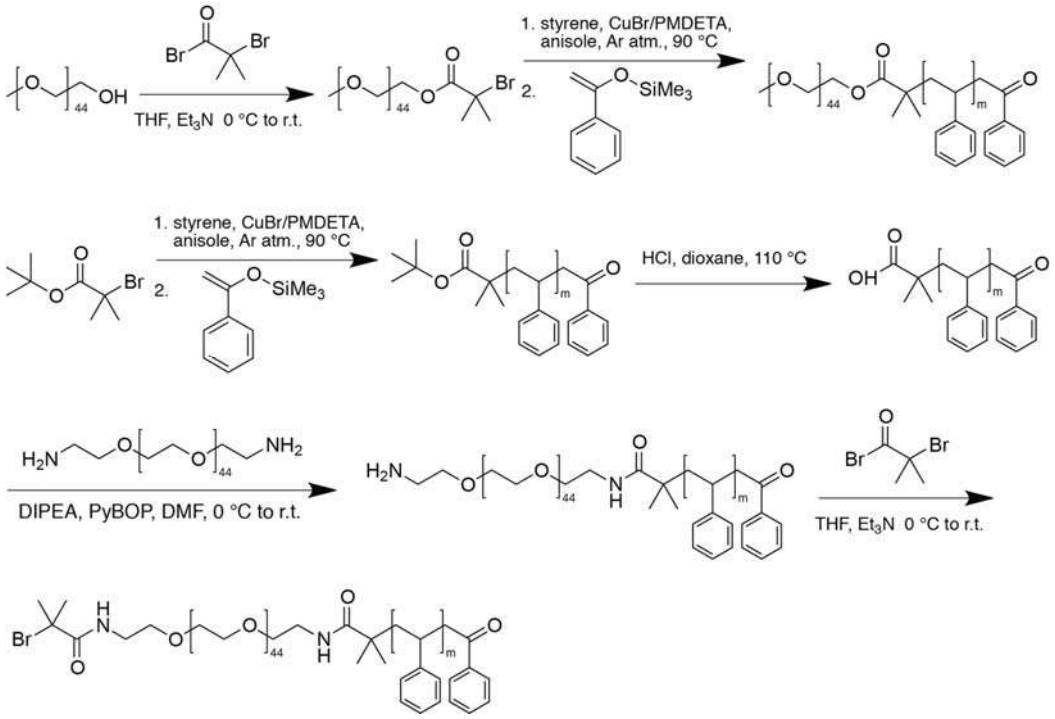


Scheme 1 Synthetic route for the block copolymer poly(ethylene glycol)-*b*-polystyrene (PEG-*b*-PS) and α-bromo ester functional-poly(ethylene glycol)-*b*-polystyrene (Br-PEG-*b*-PS) via ATRP protocol.

***Synthesis of α-methoxy-poly(ethylene glycol)$_{44}$ ATRP macromolecular initiator (1)***

Poly(ethylene glycol) methyl ether (5.00 g, 2.50 mmol) was dried by co-evaporation with toluene.

The polymer was dissolved in freshly distilled THF in a flamed-dried Schlenk flask. After adding triethylamine (1.04 mL, 7.50 mmol), the mixture was cooled to 0 °C. α-bromoisobutyryl bromide (616 μL, 5.00 mmol) was added dropwise. After addition, the resulting solution was stirred for 24h while slowly warming to room temperature. After the reaction, the white precipitate was filtered off and the solution was concentrated. The polymer was precipitated in ice-cold diethyl ether (2x). The polymer was characterized by $^1$H-NMR in $CDCl_3$.

$^1$H-NMR (400 MHZ, $CDCl_3$) δ: 4.33 (t, 2H, $CH_2CH_2OC(O)C(CH_3)_2Br$), 3.76 (t, 2H, $CH_2CH_2OC(O)C(CH_3)_2Br$), 3.65 (br. s, PEG backbone), 3.55 (m, 2H, $CH_3OCH_2$), 3.38 (s, 3H, $CH_3OCH_2$), 1.94 (s, 6H, $C(CH_3)_2Br$) ppm.

***Synthesis of poly(ethylene glycol)-b-polystyrene (2)***

The Schlenk tube with CuBr (45 mg, 0.32 mmol) was evacuated for 15 min and refilled with Ar for three times. PMDETA (66 μL, 0.32 mmol) in anisole (0.5 mL) was added, followed by 15 min vigorously stirring. Styrene (5 mL, 43.6 mmol) in anisole (0.5 mL) was added via a syringe and degassed for 15 min. After cooling the mixture to 0 °C, PEG-initiator (215 mg, 0.1 mmol) dissolved in anisole (0.5 mL) was injected and the solution was degassed for another 15 min. The Schlenk tube was transferred into an oil bath at 90 °C. $^1$H-NMR was used for monitoring the reaction process. Upon attainment of the required molecular weight, 1-phenyl-1-trimethylsiloxyethene (1.91 mL, 9.28 mmol) was added to quench the polymerization. The reaction was terminated by cooling to room temperature after stirring for 2h. The solution was diluted with $CH_2Cl_2$ and extracted with an aqueous EDTA solution (65 mM). The organic layer was collected and dried with $MgSO_4$ and concentrated. The polymer was obtained after precipitation in MeOH (3x) and dried under vacuum overnight. The polymer was characterized by $^1$H-NMR in $CDCl_3$.

$^1$H-NMR (400 MHZ, $CDCl_3$) δ: 7.20-6.30 (br. s, PS arom.), 3.64 (br. s, PEG backbone), 3.38 (s, 3H, $CH_3OCH_2$), 2.30-1.20 (br. s, PS backbone), 0.90 (br. m, 6H, $C(O)C(CH_3)_2CH_2$) ppm.

***Synthesis of α-tert-Butyloxycarbonyl-polystyrene (3)***

The Schlenk tube with CuBr (45 mg, 0.32 mmol) was evacuated for 15min and refilled with Ar for three times. PMDETA (66 μL, 0.32 mmol) in anisole (0.5 mL) was added, followed by 15 min vigorously stirring. Styrene (5.74 mL, 50 mmol) in anisole (0.5 mL) was added via a syringe

and degassed for 15 min. After cooling the mixture to 0 °C, *tert*-butyl α-bromoisobutyrate (27 μL, 0.14 mmol) in anisole was injected and the solution was degassed for another 15 min. The Schlenk tube was transferred into an oil bath at 90 °C. $^1$H-NMR was used for monitoring the reaction process. Upon attainment of the required molecular weight, the reaction was terminated by adding 1-phenyl-1-trimethylsiloxyethene (1.91 mL, 9.28 mmol). The mixture was stirred for 2h. The solution was diluted with $CH_2Cl_2$ and extracted with an aqueous solution of EDTA (65 mM). The organic layer was collected and dried with $MgSO_4$ and concentrated. The polymer was obtained after precipitation in MeOH (3x) and dried under vacuum overnight. The polymer was characterized by $^1$H-NMR in $CDCl_3$.

$^1$H-NMR (400 MHZ, $CDCl_3$) δ: 7.20-6.30 (br. s, PS arom.), 2.30-1.20 (br. s, PS backbone), 1.25 (br. m, 9H, $C(CH_3)_3$), 0.92 (br. m, 6H, $C(O)C(CH_3)_2CH_2$) ppm.

***Synthesis of α-Carboxylic acid-polystyrene (4)***

Polymer **3** (3 g) was dissolved in 1,4-dioxane (30 mL) and concentrated HCl (1.5 mL, 37%) was added. The reaction was refluxed at 110 °C overnight. The mixture was dried using a rotary evaporator and then dissolved in $CH_2Cl_2$. The polymer was obtained after precipitation in MeOH (3x) and then dried under vacuum overnight. The polymer was characterized by $^1$H-NMR in $CDCl_3$.

$^1$H-NMR (400 MHZ, $CDCl_3$) δ: 7.20-6.30 (br. s, PS arom.), 2.30-1.20 (br. s, PS backbone), 0.96 (br. m, 6H, $C(O)C(CH_3)_2CH_2$) ppm.

***Synthesis of α-amino-poly(ethylene glycol)-b-polystyrene (5)***

Polymer **4** (1 g, 43.5 μmol), α-ω-amino-poly(ethylene glycol) (521.7 mg, 260 μmol) and DIPEA (17.4 μL, 100 μmol) were dissolved in DMF (12 mL). The solution was cooled to 0 °C and PyBOP (42 mg, 80 μmol) was added. The reaction was stirred overnight, while slowly warming to room temperature. The progress of the coupling was monitored by GPC. After that, the mixture was diluted with $CH_2Cl_2$ and extracted with $NaHCO_3$ solution (4 wt%) and saturated NaCl solution. The organic layer was collected and dried with $MgSO_4$ and concentrated. The polymer was obtained after precipitation in MeOH (3x) and dried under vacuum overnight. The final polymer was characterized by $^1$H-NMR in $CDCl_3$.

$^1$H-NMR (400 MHZ, $CDCl_3$) δ: 7.20-6.30 (br. s, PS arom.), 3.64 (br. s, PEG backbone), 2.30-

1.20 (br. s, PS backbone), 0.88 (br. m, 6H, $C(O)C(CH_3)_2CH_2$) ppm.

***Synthesis of polystyrene-b-poly(ethylene glycol)-ω-bromoisobutyramide (6)***

Polymer **5** (500 mg, 20 μmol) was dissolved in 15 mL freshly distilled THF in a flame-dried Schlenk tube. After adding TEA (104 μL, 750 μmol), the mixture was cooled to 0 °C. α-bromoisobutyryl bromide (61.6 μM, 500 μmol) was added dropwise. After addition, the resulting solution was stirred for 24h while slowly warming to room temperature. After the reaction, the white precipitate was filtered off and the solution was concentrated. The polymer was precipitated in ice-cold MeOH(3x). The polymer was characterized by $^1$H-NMR in $CDCl_3$.

$^1$H-NMR (400 MHZ, $CDCl_3$) δ: 7.20-6.30 (br. s, PS arom.), 3.64 (br. s, PEG backbone), 2.30-1.20 (br. s, PS backbone), 1.96 (s, 6H, $C(CH_3)_2Br$), 0.90 (br. m, 6H, $C(O)C(CH_3)_2CH_2$) ppm.

***Heteronuclear Multiple Bond Correlation (HMBC) measurement***

The HMBC experiment measured correlations between carbons and protons that are separated by two, three, and, sometimes in conjugated systems, four bonds. In order to confirm Br was covalently attached to polymer, 5 mg Br-PEG-*b*-PS/α-bromoisobutyryl bromide was fully dissolved in 0.5 mL $CDCl_3$ and measured by HMBC. The HMBC experiment was performed with 2-fold J-filter set to 120 Hz and 170 Hz and optimized for a 10 Hz long-range C-H coupling. The experiment was performed under constant time in order to minimize the effect of relaxation. The size acquired was 2048x256 and then processed with zero-filling to 4096x512. After measurement, the difference between the HMBC signal of correlation from Br-PEG-*b*-PS and that of α-bromoisobutyryl bromide was compared in Figure 2.

***Preparation of PtNPs with PVP coating***

4 mL $K_2PtCl_4$ solution (20 mM) was added into 40 mg PVP, followed by 48 hours stirring. After that, 35 mg *L* (+) ascorbic acid in 1 mL of MilliQ water was added into the solution. The resulting solution was sonicated (VWR Ultrasonic Cleaner Model 75D) at room temperature for 1 h. The PtNPs were characterized by TEM.

***Self-assembly of Stoma or Stoma-Br***

10 mg PEG-*b*-PS (or 9 mg PEG-*b*-PS and 1mg Br-PEG-*b*-PS) was fully dissolved in 1 mL mixture of THF/dioxane (4:1, v/v). 1 mL of MilliQ water was slowly added into the solution by

a syringe pump at a rate of 1 mL/h. After vigorous dialysis for at least 48 hours, Stoma/Stoma-Br was obtained.

***Self-assembly of PtNPs-Stoma or PtNPs-Stoma-Br***

10 mg PEG-*b*-PS (or 9 mg PEG-*b*-PS and 1mg Br-PEG-*b*-PS) was fully dissolved in 1 mL mixture of THF/dioxane (4:1, v/v). 0.35 mL of MilliQ water was slowly added by a syringe pump at a rate of 1 mL/h, followed by addition of preformed PtNPs solution (0.65 mL) also at a rate of 1 mL/h. After dialysis for at least 48 hours, PtNPs-Stoma or PtNPs-Stoma-Br was obtained.

***Growing PNIPAM brushes on the surface of Stoma-Br or PtNPs-Stoma-Br***

A Schlenk flask was charged with CuBr (14.32 mg) and a stirring bar and purged with Ar for 30 min to remove oxygen. NIPAM (1.152 g) was dissolved in 10% methanol/water solution (V/V, 4 mL in total) and 62.4 μL PMDETA was added. After 30 min degassing, the NIPAM solution was transferred to the CuBr flask, followed by another 30 min degassing. 1 mL solution of the above mixture was added to 1 mL Stoma-Br solution (or PtNPs-Stoma-Br solution, 5 mg/mL polymer), which was degassed already for 30 min, and the resulting solution was stirred for 30 min at room temperature under Ar. The solution was transferred immediately into a dialysis bag and dialyzed against water with the dialysis water changed after one hour, and further frequent changes for 2 days to remove monomer.

***Size change after growing PNIPAM brushes***

The sizes and size distributions of PtNPs-Stoma, PtNPs-Stoma-Br, PtNPs-Stoma and PtNPs-Stoma-Br after SI-ATRP (PtNPs-Stoma without Br after SI-ATRP as a control) were measured respectively by a Malvern DLS-Zetasizer. (Table 1)

***NMR Calculation for Molecular Weight of PNIPAM Brush***

In order to calculate the length of PNIPAM brushes, a sample of Stoma-Brush was freeze-dried and re-dissolved in $CDCl_3$ for $^1$H-NMR measurements. The molecular weight of PNIPAM was calculated according to the ratio between NMR integration of PNIAPM and PS.

$^1$H-NMR (400 MHZ, $CDCl_3$) δ: 7.20-6.30 (br. s, PS arom.), 4.00 (br. s, PNIPAM, NHCH($CH_3$)$_2$), 3.64 (br. s, PEG backbone), 2.30-1.20 (br. s, PS backbone), 1.14 (br. s, PNIPAM, NHCH($CH_3$)$_2$) ppm.

***Stability of stomatocytes in methanol***

In order to check the stability of stomatocytes in MeOH, the sample was suspended in MeOH. TEM samples were made and analyzed.

***Diffusion NMR Measurements***

A Bruker DMX 500 MHz NMR was used for Diffusion NMR measurements. Diffusion NMR experiments resolve different compounds spectroscopically in a mixture based on their differing diffusion coefficients, depending on the size and shape of the molecules. Free PNIPAM with different molecular weight, Stoma mixed with PNIPAM and Stoma-Brush in MeOD were measured respectively and diffusion coefficients were calculated according to the equation B+exp(-x*F) (Mono-exponential Fit). (Figure 5)

***FT-IR Measurements***

Bruker TENSOR 27 was used for IR measurements. Empty Stoma, Stoma-Br, Stoma without Br modification after SI-ATRP and Stoma-Brush solution were measured respectively.

***Mixing Stoma and Stoma-Brush with Nile Red***

To demonstrate that a collapsed hydrophobic layer was formed around the stomatocyte when the particles were heated above the LCST of PNIPAM the hydrophobic dye Nile red was used. Nile red is almost non-fluorescent in water but undergoes fluorescence enhancement and large absorption and emission blue shifts in hydrophobic environments.

5 μL Nile red in DMF (6 mg/mL) was mixed with 100 μL Stoma-Brush ($3.8 \times 10^{11}$ particles/mL, measured by Nanosight) and also with normal Stoma ($3.9 \times 10^{11}$ particles/mL, measured by Nanosight) respectively, and the fluorescence intensities of both samples were measured at 30 °C by a fluorescence spectrometer (Perkin Elmer LS53). The intensities were also measured when the whole system was heated to 40 °C (above the LCST of PNIPAM). After cooling the system back to 30 °C, the intensities of both samples were measured again. (Figure 7)

***Movement Analysis***

Nanoparticle Tracking Analysis (NS 500) from Nanosight was used to record the movement of the motors for 90 seconds (30 frames per second) at different temperatures. PtNPs-Stoma without $H_2O_2$ fuel, PtNPs-Stoma with $H_2O_2$, PtNPs-Stoma-Brush without $H_2O_2$ and PtNPs-Stoma-Brush

with $H_2O_2$ were measured respectively. Theoretical calculation of the rotational diffusion of the particles via the equation $D_r \approx k_B T/(8\pi\eta r^3)$ gave a calculated value of 7.3 per seconds, which is much smaller than the frame rate. The fitting of the MSD allows for calculation of the speed of the nanomotors by using the self-diffusiophoretic model proposed by Golestanian and coworkers. While a purely diffusive system would show only a linear component according to $(4D)\Delta t$ equation from which an enhanced diffusion coefficient can be extracted, our MSD curves are not linear and show a parabolic fit according to the equation $(4D)\Delta t + (v^2)(\Delta t^2)$ from which we can extract the velocity of the particles. Chemotaxis and Migration Tool 2.0 from Ibidi Company was used for directionality calculation. Mean square displacement (MSD), directionality and MSD fitting can be seen in Figure 8 and Figure 9.

$$\text{Directionality} = \frac{1}{n}\sum_{i=1}^{n} \text{Di} = \frac{1}{n}\sum_{i=1}^{n} \frac{\text{d}i, euclid}{\text{d}i, accum}$$

***Catalytic Efficiency of PtNPs***

In order to figure out the reason why PtNPs-Stoma-Brush move faster after one cycle, the catalytic efficiency of PtNPs was measured *via* the 3,3',5,5'-tetramethylbenzidine (TMB)-$H_2O_2$ reaction. PtNPs are shown to have activity that can be monitored colorimetrically by the color change seen from the oxidation of TMB to its one-electron oxidation product. 50 μL TMB (dissolved in DMSO, 4 mg/mL) and 50 μL $H_2O_2$ solution (5%) were added into 900 μL citric buffer (pH=4.0) as working solution. 10 μL PtNPs solution, PtNPs solution after one cycle, PtNPs solution after two cycles and PtNPs solution after three cycles were added respectively into 240 μL working solution and UV absorbance was measured afterwards, which was related to catalytic efficiency of PtNPs. The absorbances of the samples were compared in Figure 11.

## 6 References


1. Sengupta, S., *et al.* Self-powered enzyme micropumps. *Nat. Chem.* **6**, 415-422 (2014).
2. Li, J., *et al.* Nanomotor lithography. *Nat. Commun.* **5**, 5026 (2014).
3. Wang, J. *Nanomachines: fundamentals and applications*, (John Wiley & Sons, 2013).

4. Guix, M., Mayorga-Martinez, C.C. & Merkoci, A. Nano/micromotors in (bio)chemical science applications. *Chem. Rev.* **114**, 6285-6322 (2014).
5. Wang, J. & Gao, W. Nano/Microscale motors: biomedical opportunities and challenges. *ACS Nano* **6**, 5745-5751 (2012).
6. Abdelmohsen, L.K.E.A., Peng, F., Tu, Y. & Wilson, D.A. Micro- and nano-motors for biomedical applications. *J. Mater. Chem. B* **2**, 2395-2408 (2014).
7. Sengupta, S., Ibele, M.E. & Sen, A. Fantastic voyage: designing self-powered nanorobots. *Angew. Chem. Int. Ed.* **51**, 8434-8445 (2012).
8. Peng, F., Tu, Y., van Hest, J.C.M. & Wilson, D.A. Self□guided supramolecular cargo□loaded nanomotors with chemotactic behavior towards cells. *Angew. Chem. Int. Ed.* **127**, 11828-11831 (2015).
9. Tu, Y.*, et al.* Mimicking the cell: bio-inspired functions of supramolecular assemblies. *Chem. Rev.* **116**, 2023-2078 (2015).
10. Ismagilov, R.F., Schwartz, A., Bowden, N. & Whitesides, G.M. Autonomous movement and self□assembly. *Angew. Chem. Int. Ed.* **114**, 674-676 (2002).
11. Mei, Y.*, et al.* Versatile approach for integrative and functionalized tubes by strain engineering of nanomembranes on polymers. *Adv. Mater.* **20**, 4085-4090 (2008).
12. Sánchez, S.*, et al.* Tubular micro-nanorobots: smart design for bio-related applications. in *Small-scale robotics. From nano-to-millimeter-sized robotic systems and applications* 16-27 (Springer, 2014).
13. Gao, W., Sattayasamitsathit, S., Orozco, J. & Wang, J. Highly efficient catalytic microengines: template electrosynthesis of polyaniline/platinum microtubes. *J. Am. Chem. Soc.* **133**, 11862-11864 (2011).
14. Soler, L., Magdanz, V., Fomin, V.M., Sanchez, S. & Schmidt, O.G. Self-propelled micromotors for cleaning polluted water. *ACS Nano* **7**, 9611-9620 (2013).
15. Zhang, L.*, et al.* Controlled propulsion and cargo transport of rotating nickel nanowires near a patterned solid surface. *ACS Nano* **4**, 6228-6234 (2010).
16. Gao, W., Sattayasamitsathit, S., Manesh, K.M., Weihs, D. & Wang, J. Magnetically powered flexible metal nanowire motors. *J. Am. Chem. Soc.* **132**, 14403-14405 (2010).
17. Zhang, L.*, et al.* Artificial bacterial flagella: fabrication and magnetic control. *Appl. Phys.*

*Lett.* **94**, 064107 (2009).

18. Zhang, L.*, et al.* Characterizing the swimming properties of artificial bacterial flagella. *Nano Lett.* **9**, 3663-3667 (2009).
19. Wang, W., Castro, L.A., Hoyos, M. & Mallouk, T.E. Autonomous motion of metallic microrods propelled by ultrasound. *ACS Nano* **6**, 6122-6132 (2012).
20. Wang, W.*, et al.* Acoustic propulsion of nanorod motors inside living cells. *Angew. Chem. Int. Ed.* **53**, 3201-3204 (2014).
21. Paxton, W.F.*, et al.* Catalytic nanomotors: autonomous movement of striped nanorods. *J. Am. Chem. Soc.* **126**, 13424-13431 (2004).
22. Pavlick, R.A., Sengupta, S., McFadden, T., Zhang, H. & Sen, A. A polymerization□ powered motor. *Angew. Chem. Int. Ed.* **123**, 9546-9549 (2011).
23. Baraban, L.*, et al.* Catalytic Janus motors on microfluidic chip: deterministic motion for targeted cargo delivery. *ACS Nano* **6**, 3383-3389 (2012).
24. Ma, X.*, et al.* Enzyme-powered hollow mesoporous Janus nanomotors. *Nano Lett.* **15**, 7043-7050 (2015).
25. Wilson, D.A., Nolte, R.J. & van Hest, J.C.M. Autonomous movement of platinum-loaded stomatocytes. *Nat. Chem.* **4**, 268-274 (2012).
26. Wu, Y., Wu, Z., Lin, X., He, Q. & Li, J. Autonomous movement of controllable assembled Janus capsule motors. *ACS Nano* **6**, 10910-10916 (2012).
27. Abdelmohsen, L.K.*, et al.* Dynamic loading and unloading of proteins in polymeric stomatocytes: formation of enzyme-loaded supramolecular nanomotor. *ACS Nano* **10**, 2652-2660 (2016).
28. Kline, T.R., Paxton, W.F., Mallouk, T.E. & Sen, A. Catalytic nanomotors: remote□ controlled autonomous movement of striped metallic nanorods. *Angew. Chem. Int. Ed.* **117**, 754-756 (2005).
29. Ma, X., Hahn, K. & Sanchez, S. Catalytic mesoporous Janus nanomotors for active cargo delivery. *J. Am. Chem. Soc.* **137**, 4976-4979 (2015).
30. Sanchez, S., Solovev, A.A., Mei, Y. & Schmidt, O.G. Dynamics of biocatalytic microengines mediated by variable friction control. *J. Am. Chem. Soc.* **132**, 13144-13145 (2010).

31. Laocharoensuk, R., Burdick, J. & Wang, J. Carbon-nanotube-induced acceleration of catalytic nanomotors. *ACS Nano* **2**, 1069-1075 (2008).
32. Baylis, J.R.*, et al.* Self-propelled particles that transport cargo through flowing blood and halt hemorrhage. *Sci. Adv.* **1**, e1500379 (2015).
33. Gao, W., Uygun, A. & Wang, J. Hydrogen-bubble-propelled zinc-based microrockets in strongly acidic media. *J. Am. Chem. Soc.* **134**, 897-900 (2011).
34. Gao, W., Pei, A. & Wang, J. Water-driven micromotors. *ACS Nano* **6**, 8432-8438 (2012).
35. Pantarotto, D., Browne, W.R. & Feringa, B.L. Autonomous propulsion of carbon nanotubes powered by a multienzyme ensemble. *Chem. Commun.*, 1533-1535 (2008).
36. Tottori, S.*, et al.* Magnetic helical micromachines: fabrication, controlled swimming, and cargo transport. *Adv. Mater.* **24**, 811-816 (2012).
37. Sing, C.E., Schmid, L., Schneider, M.F., Franke, T. & Alexander-Katz, A. Controlled surface-induced flows from the motion of self-assembled colloidal walkers. *Proc. Natl. Acad. Sci. U.S.A.* **107**, 535-540 (2010).
38. Garcia-Gradilla, V.*, et al.* Functionalized ultrasound-propelled magnetically guided nanomotors: Toward practical biomedical applications. *ACS Nano* **7**, 9232-9240 (2013).
39. Chang, S.T., Paunov, V.N., Petsev, D.N. & Velev, O.D. Remotely powered self-propelling particles and micropumps based on miniature diodes. *Nat. Mater.* **6**, 235-240 (2007).
40. Loget, G. & Kuhn, A. Electric field-induced chemical locomotion of conducting objects. *Nat. Commun.* **2**, 535 (2011).
41. Ibele, M., Mallouk, T.E. & Sen, A. Schooling behavior of light□powered autonomous micromotors in water. *Angew. Chem. Int. Ed.* **48**, 3308-3312 (2009).
42. Ichimura, K., Oh, S.-K. & Nakagawa, M. Light-driven motion of liquids on a photoresponsive surface. *Science* **288**, 1624-1626 (2000).
43. Hong, Y., Diaz, M., Córdova□Figueroa, U.M. & Sen, A. Light□driven titanium□dioxide□based reversible microfireworks and micromotor/micropump systems. *Adv. Funct. Mater.* **20**, 1568-1576 (2010).
44. Magdanz, V., Sanchez, S. & Schmidt, O.G. Development of a sperm□flagella driven micro□bio□robot. *Adv. Mater.* **25**, 6581-6588 (2013).
45. Mirkovic, T., Zacharia, N.S., Scholes, G.D. & Ozin, G.A. Fuel for thought: chemically

powered nanomotors out-swim nature's flagellated bacteria. *ACS Nano* **4**, 1782-1789 (2010).

46. Balasubramanian, S.*, et al.* Thermal modulation of nanomotor movement. *Small* **5**, 1569-1574 (2009).

47. Magdanz, V., Stoychev, G., Ionov, L., Sanchez, S. & Schmidt, O. Stimuli□responsive microjets with reconfigurable shape. *Angew. Chem. Int. Ed.* **53**, 2673-2677 (2014).

48. Wu, Z.*, et al.* Near-infrared light-triggered "on/off" motion of polymer multilayer rockets. *ACS Nano* **8**, 6097-6105 (2014).

49. Ma, X., Wang, X., Hahn, K. & Sánchez, S. Motion control of urea-powered biocompatible hollow microcapsules. *ACS Nano* **10**, 3597-3605 (2016).

50. Li, Z., Barnes, J.C., Bosoy, A., Stoddart, J.F. & Zink, J.I. Mesoporous silica nanoparticles in biomedical applications. *Chem. Soc. Rev.* **41**, 2590-2605 (2012).

51. Szatrowski, T.P. & Nathan, C.F. Production of large amounts of hydrogen peroxide by human tumor cells. *Cancer Res.* **51**, 794-798 (1991).

52. Chen, T., Ferris, R., Zhang, J., Ducker, R. & Zauscher, S. Stimulus-responsive polymer brushes on surfaces: transduction mechanisms and applications. *Prog. Polym. Sci.* **35**, 94-112 (2010).

53. Zhang, X.*, et al.* Multifunctional up□converting nanocomposites with smart polymer brushes gated mesopores for cell imaging and thermo/pH dual□responsive drug controlled release. *Adv. Funct. Mater.* **23**, 4067-4078 (2013).

54. Sui, X.*, et al.* Stability and cell adhesion properties of poly (N-isopropylacrylamide) brushes with variable grafting densities. *Aust. J. Chem.* **64**, 1261-1268 (2011).

55. Liu, H.*, et al.* Dual-responsive surfaces modified with phenylboronic acid-containing polymer brush to reversibly capture and release cancer cells. *J. Am. Chem. Soc.* **135**, 7603-7609 (2013).

56. Stuart, M.A.C.*, et al.* Emerging applications of stimuli-responsive polymer materials. *Nat. Mater.* **9**, 101-113 (2010).

57. Barbey, R.*, et al.* Polymer brushes via surface-initiated controlled radical polymerization: synthesis, characterization, properties, and applications. *Chem. Rev.* **109**, 5437-5527 (2009).

58. Schild, H.G. Poly (N-isopropylacrylamide): experiment, theory and application. *Prog. Polym. Sci.* **17**, 163-249 (1992).

59. Shi, S., *et al.* Poly (N-isopropylacrylamide)-Au hybrid microgels: synthesis, characterization, thermally tunable optical and catalytic properties. *Soft Matter* **9**, 10966-10970 (2013).

60. Howse, J.R., *et al.* Self-motile colloidal particles: from directed propulsion to random walk. *Phys. Rev. Lett.* **99**, 048102 (2007).

61. Wilson, D.A., Nijs, B., Blaaderen, A., Nolte, R.J. & van Hest, J.C.M. Fuel concentration dependent movement of supramolecular catalytic nanomotors. *Nanoscale* **5**, 1315-1318 (2013).

62. Wang, S. & Wu, N. Selecting the swimming mechanisms of colloidal particles: bubble propulsion versus self-diffusiophoresis. *Langmuir* **30**, 3477-3486 (2014).